Chemical Science

RSC Publishing

EDGE ARTICLE

Exploring quantum phenomena and vibrational control in σ* mediated photochemistry†

Cite this: *Chem. Sci.*, 2013, **4**, 993

Gareth M. Roberts,[a] David J. Hadden,[a] L. Therese Bergendahl,[b] Andreas M. Wenge,[c] Stephanie J. Harris,[c] Tolga N. V. Karsili,[c] Michael N. R. Ashfold,*[c] Martin J. Paterson*[b] and Vasilios G. Stavros*[a]

Received 31st October 2012
Accepted 29th November 2012

DOI: 10.1039/c2sc21865h

www.rsc.org/chemicalscience

Non-adiabatic dynamics involving $^1\pi\sigma^*$ or $^1n\sigma^*$ excited electronic states play a key role in the photochemistry of numerous heteroatom containing aromatic (bio-)molecules. In this contribution, we investigate more exotic phenomena involved in σ* mediated dynamics, namely: (i) the role of purely quantum mechanical behavior; and (ii) manipulating non-adiabatic photochemistry through conical intersections (CIs) with 'vibration-specific control'. This is achieved by investigating S–CH_3 bond fission *via* a $^1n\sigma^*$ potential energy surface (PES) in thioanisole ($C_6H_5SCH_3$). Using a combination of time- and frequency-resolved velocity map ion imaging techniques, together with *ab initio* calculations, we demonstrate that excitation to the $^1\pi\pi^* \leftarrow S_0$ origin [$^1\pi\pi^*(\nu = 0)$] results in S–CH_3 bond fission on the $^1n\sigma^*$ PES, despite an (apparent) energetic barrier to dissociation formed by a CI between the $^1\pi\pi^*$ and $^1n\sigma^*$ PESs. This process occurs by accessing 'classically forbidden' regions of the excited state potential energy landscape where the barrier to dissociation becomes negligible, aided by torsional motion of the S–CH_3 group out of the plane of the phenyl ring. Control over these dynamics is attained by populating a single quantum of the S–CH_3 stretch mode in the $^1\pi\pi^*$ state [$^1\pi\pi^*(\nu_{7a} = 1)$], which mirrors the nuclear motion required to promote coupling through the $^1\pi\pi^*/^1n\sigma^*$ CI, resulting in a marked change in the electronic branching in the C_6H_5S radical products. This observation offers an elegant contribution towards a vision of 'quantum control' in photo-initiated chemical reaction dynamics.

1 Introduction

In recent years, non-adiabatic dynamics at conical intersections (CIs)[1,2] have become a centerpiece for understanding exceptionally efficient radiationless relaxation mechanisms in many heteroatom-containing aromatic species, *e.g.* phenols, indoles and azoles.[3,4] Such molecules act as ultraviolet (UV) chromophores in a variety of 'photostable' biomolecules, including DNA nucleobases and aromatic amino acids – species notorious for displaying low fluorescence quantum yields and an aversion to excited state photoreactions.[5] Specifically, contemporary research has begun to illuminate the role that optically 'dark' dissociative excited states (which exhibit notable anti-bonding σ* character) can play in dissipating harmful excess UV energy when coupled to optically 'bright' $^1\pi\pi^*$ potential energy surfaces (PESs) *via* CIs.[3,4] These dynamics are typically localized along heteroatom-hydride bonds (X–H, where X = O, N or S), resulting in either ultrafast repopulation of the electronic ground state (S_0) through an appropriate CI, effectively transforming potentially toxic UV photon energy into heat (vibrational energy in S_0), or highly specific X–H bond fission and the formation of radical photoproducts. Moreover, it has been postulated that ultrafast dynamics on $^1\pi\sigma^*$ and $^1n\sigma^*$ PESs may be key to reducing the lifetimes of excited states that could otherwise lead to toxic processes in biological systems,[3] contributing to the remarkable resilience many heteroatom containing aromatic biomolecules display with respect to UV induced photodegradation. In addition to their proposed role in fundamental photobiology, σ* mediated dynamics contribute to wider aspects of excited state photochemistry, and can also be active in both aromatic and aliphatic molecules along X–Y/R bond coordinates (Y = halogen, R = alkyl group),[6–8] broadening the significance of this behavior to encompass a myriad of chemical species.[4]

In this work, we turn our attention to understanding more exotic aspects of photochemistry driven by (n/π)σ* excited states, with particular focus on: (i) the ways in which specific vibrations can promote/control non-adiabatic processes through CIs; and (ii) the role purely quantum mechanical phenomena play in these dynamics – specifically the penetration of vibrational wavefunctions into classically forbidden regions of the potential

[a]*Department of Chemistry, University of Warwick, Library Road, Coventry, CV4 7AL, UK. E-mail: v.stavros@warwick.ac.uk*

[b]*Institute of Chemical Sciences, Heriot-Watt University, Edinburgh, EH14 4AS, UK. E-mail: m.j.paterson@hw.ac.uk*

[c]*School of Chemistry, University of Bristol, Bristol, BS8 1TS UK. E-mail: mike.ashfold@bristol.ac.uk*

† Electronic supplementary information (ESI) available. See DOI: 10.1039/c2sc21865h

energy landscape (*i.e.* tunneling). This is achieved by interrogating $^1n\sigma^*$ state mediated S–CH_3 fission dynamics in thioanisole (Fig. 1).

$^1n\sigma^*$ state mediated S–CH_3 bond cleavage in thioanisole has already been shown[9] to proceed in a manner qualitatively similar to $^1\pi\sigma^*$ governed S–H bond fission dynamics in thiophenols (C_6H_5SH), which have received more attention in both the gas[10–13] and solution phases.[14,15] With respect to the schematic PESs depicted in Fig. 1, after initial excitation of thioanisole to its $^1\pi\pi^*$ state with a pump laser photon of frequency ν_{pu}, excited state population may couple onto a dissociative $^1n\sigma^*$ PES and evolve to radical photoproducts:

$$\begin{aligned} C_6H_5S-CH_3 \; + \; h\nu_{pu} \rightarrow \\ C_6H_5S(\tilde{X}) \; + \; CH_3 \; [1] \\ C_6H_5S(\tilde{A}) \; + \; CH_3 \; [2] \end{aligned} \qquad (1)$$

Recent velocity map ion imaging (VMI) experiments by Lim and Kim[9] following nanosecond (ns) laser excitation at the $^1\pi\pi^* \leftarrow S_0$ band origin [$^1\pi\pi^*(\nu = 0)$] suggest that a small fraction (~5%) of the dissociating flux undergoes non-adiabatic coupling through the $^1n\sigma^*/S_0$ CI (hereon designated CI2) to yield $C_6H_5S(\tilde{X})$ + CH_3 products, while the remainder evolves adiabatically, avoiding CI2 and yielding $C_6H_5S(\tilde{A})$ + CH_3 radicals; these two dissociation pathways are labeled channels 1 and 2, respectively, in Fig. 1 and eqn (1). The dominance of adiabatic dynamics was qualitatively interpreted by these authors in terms of the geometric phase effect,[16] where the dissociating flux bifurcates around CI2, destructively interferes and diminishes the population evolving non-adiabatically into channel 1. Lim and Kim also identified an anomalous 'dynamic resonance' when exciting an $^1\pi\pi^* \leftarrow S_0$ feature at 283.9 nm – assigned to population of the in-plane C–S–CH_3 stretch mode (labeled ν_{7a} in Varsányi's notation[17]) lying 722 cm^{-1} above the $^1\pi\pi^*$ origin [*i.e.* the $^1\pi\pi^*(\nu_{7a} = 1)$ level] – resulting in a striking enhancement of the relative yield of channel 1 photoproducts;[9] such behavior is reminiscent of that found in previous ground state mode-specific control experiments reported by Crim and co-workers in ammonia[18,19] and phenol.[20] Lim and Kim suggested that exciting at this specific wavelength led to simultaneous population of both $^1\pi\pi^*$ and $^1n\sigma^*$ states (a superposition), that the $^1n\sigma^*$ component evolved directly through the $^1\pi\pi^*/^1n\sigma^*$ CI labeled CI1′ in Fig. 1 and that the impulse along the S–CH_3 stretch coordinate (R_{S-CH_3}), induced by ν_{7a}, encouraged non-adiabatic transfer from $^1n\sigma^*$ through CI2 into channel 1 (dashed arrows labeled ν_{7a} in Fig. 1).

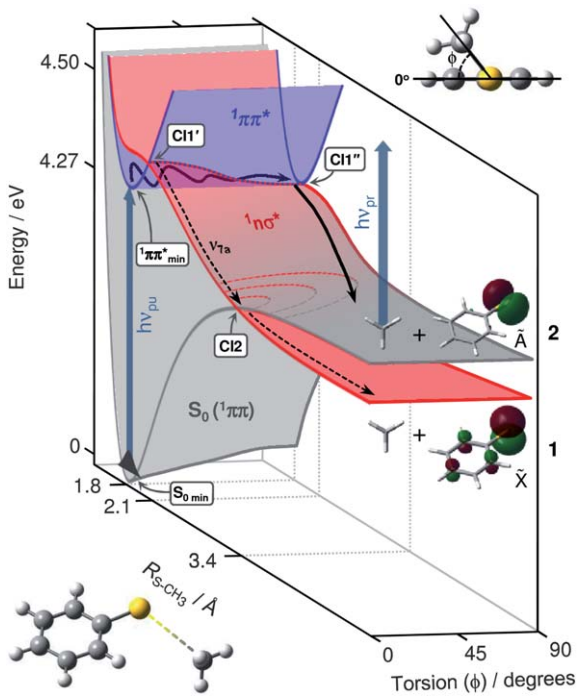

Fig. 1 Schematic of the S_0 ($^1\pi\pi$), $^1\pi\pi^*$ and $^1n\sigma^*$ singlet electronic PESs of thioanisole (structure inset), shown with respect to the S–CH_3 bond coordinate (R_{S-CH_3}) and the torsional angle (ϕ). Excitation laser pulses ($h\nu_{pu}$) and probe pulses ($h\nu_{pr}$) are indicated by vertical blue arrows. Nuclear rearrangement in ϕ (curly black arrow) enables coupling from the $^1\pi\pi^*$ to the $^1n\sigma^*$ PES and adiabatic S–CH_3 dissociation into channel 2 photoproducts (solid black arrow). Also labeled are significant nuclear geometries, associated with minima and CIs. The dotted line represents a quasi-seam of CI between the $^1\pi\pi^*$ and the $^1n\sigma^*$ PESs – see main text for further details.

The previous studies have gone some way to elucidating the origins of the intriguing fragmentation dynamics displayed by thioanisole, but many aspects remain un-assessed. For example, excitation to the $^1\pi\pi^*$ state at energies below CI1′ – *e.g.* to the $^1\pi\pi^*(\nu = 0)$ level – still yields translationally excited radical products (the signature for coupling to and dissociation on the $^1n\sigma^*$ PES), despite the implied barrier in the R_{S-CH_3} coordinate.[9] Further, there is minimal reported theoretical work directed at understanding the excited state PESs and CIs involved in these dynamics. In this report, we present results of new and comprehensive investigations of the dynamics involving the $^1n\sigma^*$ excited state of thioanisole. Our approach combines three complementary methodologies: (i) time-resolved femtosecond (fs) velocity map ion imaging (TR-VMI), which provides both temporal and energy resolution regarding the S–CH_3 dissociation process along the $^1n\sigma^*$ PES; (ii) frequency-resolved ns VMI measurements, which offer higher energy resolution and allow more detailed investigation of the fragmentation dynamics following excitation of specific $^1\pi\pi^*$ levels; and (iii) high level complete active space self consistent field (CASSCF) calculations, which characterize important attributes of the excited state PESs, in particular CIs, which govern the dynamics in question. This distinctive combination reveals key properties of the $^1\pi\pi^*/^1n\sigma^*$ CI that control the origins of the observed dynamic resonance and give rise to the striking change in the electronic branching in the photoproducts. More generally, this work also provides another elegant reminder of the sensitivity of excited state dynamics to purely quantum phenomena and the detailed topography of the multi-dimensional PESs on which the dissociation proceeds.

2 Methods

Both the ns VMI and fs TR-VMI apparatus have been described previously[21,22] and further details are provided in the electronic supplementary information (ESI†) online. Briefly, thioanisole

was obtained commercially (Sigma-Aldrich, >99%) and used without further purification. In both experiments, a vapor pressure of thioanisole (maintained at a temperature of ~60 °C) was seeded in He (0.4–2 bar) and expanded into a VMI spectrometer[23] using a pulsed solenoid valve. Seeded molecular beam pulses are intersected by either tunable ns or fs laser pulses (289.8–275 nm) which trigger photolysis. A second time-delayed (Δt) ns or fs laser pulse (333.6 nm) resonantly ionizes any $CH_3(\nu = 0)$ photoproducts by 2 + 1 resonance enhanced multiphoton ionization (REMPI),[24] forming CH_3^+. In the fs TR-VMI experiments, a variable Δt between the photolysis and ionization laser pulses is generated using a computer controlled optical delay line (Physik-Instrumente, M-521.DD), and the Gaussian laser cross-correlation is measured to be ~120 fs full width at half maximum. In the ns VMI experiments Δt is fixed at ~20 ns. CH_3^+ is analyzed using VMI and the resultant velocity map images are used to derive the desired total kinetic energy release (TKER) spectra using a polar onion-peeling algorithm,[25] together with an appropriate Jacobian and calibration factor, assuming C_6H_5S as the radical co-fragments of the dissociation process. CASSCF calculations were performed using the Gaussian 03 package[26] with further details given in the ESI† online.

3 Results and discussion

3.1 Photolysis at $^1\pi\pi^*(\nu = 0)$

The inset within Fig. 2(a) shows a velocity map image of the CH_3 radicals formed following ns laser excitation to the $^1\pi\pi^*(\nu = 0)$ level at 289.8 nm, and subsequently ionized by 2+1 REMPI at a probe wavelength of 333.6 nm. The left half displays the raw recorded image, while the right half shows a reconstructed slice through the centre of the original 3-D velocity distribution. The image provides information on both the speed and angular recoil distributions of the CH_3 radical products, with the radial distance from the center of the image proportional to the velocity. It is dominated by an anisotropic feature at large radius, which displays enhanced intensity parallel to the electric field vector of the pump laser, $\boldsymbol{\varepsilon}$ (indicated by the white arrow).

The TKER spectrum derived from this ns velocity map image is also presented (open circles in Fig. 2(a)). The solid black line shows a fit to the TKER spectrum, with the red and blue lines representing the two (assumed Gaussian) product sub-groups. The TKER spectrum is dominated by a broad peak centered at ~5800 cm^{-1}, with a second weak component (not immediately apparent from a cursory inspection of the image) at higher TKER. The measured spectrum is in reasonable accord with that reported previously at this same excitation wavelength,[9] though we note that by careful experimental optimization we have suppressed most of the underlying background signal that we attribute to excitation and dissociation of clusters (*e.g.* dimers, trimers *etc.*) within the molecular beam pulses and/or to unintended multiphoton excitations. This enables a 'cleaner' determination and analysis of the angular recoil anisotropy parameter (β_2) and its TKER dependence (see ESI†).

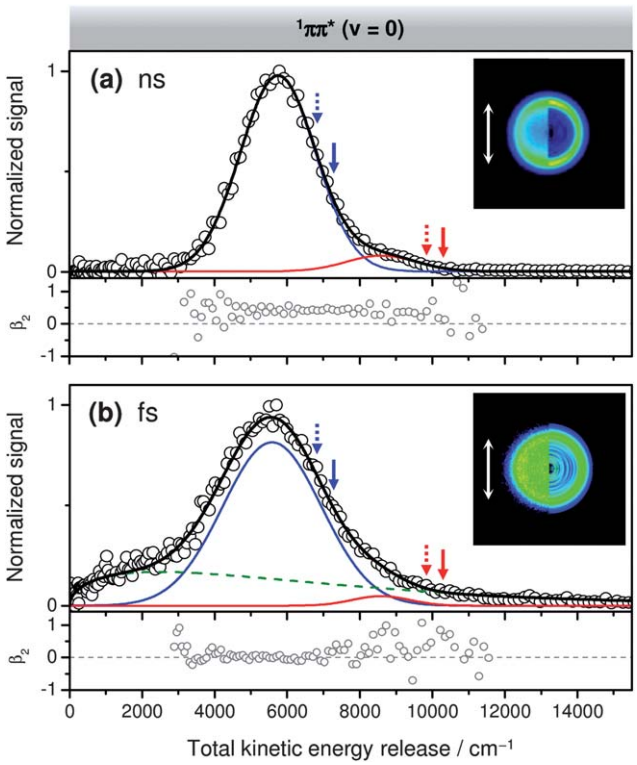

Fig. 2 TKER spectra obtained following photoexcitation of thioanisole with (a) ns and (b) fs laser pulses centered at 289.8 nm, and REMPI probing of the CH_3 radical products, recorded at Δt = 20 and 1.2 ns, respectively. Associated velocity map images from which the TKER spectra are derived are shown inset (left halves = raw recorded images, right halves = deconvoluted slices, white arrows = $\boldsymbol{\varepsilon}$). Solid black lines correspond to fits to the TKER spectra (see ESI†), with individual components of the fit associated with the channel 1 (red), channel 2 (blue) and Boltzmann-like background (dashed green) signals. Vertical red and blue arrows indicate the predicted $TKER_{max}(\tilde{X})$ and $TKER_{max}(\tilde{A})$ values extracted from eqn (2) and (3), respectively. β_2 anisotropy parameters (grey circles) extracted from the images are provided below.

The earlier VMI study[9] returned an estimate for the S–CH_3 bond dissociation energy $D_0(S\text{–}CH_3) \sim 24\,650$ cm^{-1} which, given eqn (2)

$$TKER_{max}(\tilde{X}) = h\nu_{pu} - D_0(S\text{–}CH_3), \quad (2)$$

and a $h\nu_{pu}$ energy of ~34 510 cm^{-1}, would imply a maximum TKER for channel 1 products ($TKER_{max}(\tilde{X})$) in their respective zero-point vibrational energy levels of ~9860 cm^{-1}, as indicated by the dashed vertical red arrow on the TKER spectrum in Fig. 2(a). This value matches reasonably well with the location of the smaller feature, reinforcing the view that this signal is associated with S–CH_3 bond fission along the $^1n\sigma^*$ PES into channel 1 products. The maximum TKER for photodissociation into channel 2 ($TKER_{max}(\tilde{A})$) can be attained through the relationship

$$TKER_{max}(\tilde{A}) = TKER_{max}(\tilde{X}) - \Delta E(\tilde{A} \leftarrow \tilde{X}), \quad (3)$$

where $\Delta E(\tilde{A} \leftarrow \tilde{X})$ is the energy separation between the ground $\tilde{X}$ and first excited $\tilde{A}$ states of the C_6H_5S radical co-fragments (3000 ± 7 cm^{-1}),[27] yielding an estimate of ~6860 cm^{-1} for

$TKER_{max}(\tilde{A})$ – shown by the dashed vertical blue arrow in Fig. 2(a). Though clearly supporting the previous attribution of the dominant component to $^1n\sigma^*$ mediated S–CH_3 bond fission into channel 2 products, it is also clear that neither $TKER_{max}$ predicted using the previous bond strength estimate aligns particularly well with the high energy edge of the respective fit functions. From analysis of these and other ns VMI images we propose a revised D_0(S–CH_3) ~24 400 cm^{-1}. The $TKER_{max}(\tilde{A})$ and $TKER_{max}(\tilde{X})$ values implied by this revised bond strength are indicated by the solid blue and red vertical arrows respectively in Fig. 2(a). Based on these energetics, we deduce that the $\tilde{A}$ (and $\tilde{X}$) state thiophenoxyl partners of the monitored $CH_3(\nu = 0)$ products are formed with a wide spread of internal (vibrational) energies centered at $\langle E_{vib} \rangle$ ~1500 cm^{-1}.

The foregoing assignments allow an estimation of the electronic branching ratio in the radical products, by integrating the channel 1 (red line) and 2 (blue line) fit components. Following excitation to $^1\pi\pi^*(\nu = 0)$, a branching ratio, Γ, of ~0.1 between the channel 1 : channel 2 photoproducts is obtained, where $\Gamma = \sigma[1]/\sigma[2]$ and $\sigma[1]$ and $\sigma[2]$ are the integrated channel 1 and 2 signal components, respectively. This value for Γ implies that ~10% of the dissociating flux evolves non-adiabatically through CI2 into channel 1, with the remainder following the adiabatic route into channel 2. The value for Γ obtained here is also in reasonable accord with the earlier study, which returned a channel 1 : channel 2 branching ratio of ~0.05.[9] We note that the absolute value of the product branching ratio extracted here will be sensitive to the choice of model function used to fit the fragment distribution, though the quality of the present fit suggests that the use of Gaussian TKER functions is reasonable. Finally, the lower panel in Fig. 2(a) shows the TKER dependence of the β_2 anisotropy parameter obtained by angular fitting during the image reconstruction method (grey circles).[25] As implied by visual inspection of the image, β_2 is consistently positive ($\beta_2 \approx 0.4$) across both the channel 1 and channel 2 features.

A velocity map image of the CH_3 fragments obtained by exciting thioanisole with a fs pulse centered at 289.8 nm (*i.e.* around $^1\pi\pi^*(\nu = 0)$) and subsequent 2 + 1 REMPI using a 333.6 nm fs probe pulse delayed by $\Delta t = 1.2$ ns is displayed in Fig. 2(b), along with the associated TKER spectrum. The fs imaging results show obvious similarities with the ns measurements, although some clear differences are also evident (*vide infra*). As with the ns results (Fig. 2(a)), the fs TKER spectrum (Fig. 2(b), open circles) is dominated by a feature centered around ~5600 cm^{-1} which we associate with S–CH_3 bond scission *via* the $^1n\sigma^*$ state into channel 2 products. This distribution is somewhat broader than seen through ns imaging – unsurprisingly, given the greater spectral bandwidth of the fs pump pulse (~500 cm^{-1}) – and the signal appears to ride on top of a broad 'Boltzmann-like' background signal, which has been attenuated as much as possible. The origins of this background signal are not central to the studies presented, but are ascribed primarily to multiphoton processes.[28] Unfortunately, this background signal, together with the inherently poorer energy resolution of the fs VMI method, precludes unambiguous identification of channel 1 products at TKER ~8600 cm^{-1}. Guided by the ns results (ref. 9 and Fig. 2(a)), and for consistency, we elect to fit the fs TKER spectrum in Fig. 2(b) in terms of two Gaussian functions plus a statistical distribution to model the 'Boltzmann-like' background (see ESI† for details); the overall fit is shown by the black line. Further analysis of this fit implies an estimated branching ratio between channel 1 : channel 2 products of $\Gamma \sim 0.03$ following fs excitation around $^1\pi\pi^*(\nu = 0)$.

In contrast to the ns image in Fig. 2(a), the fs image appears isotropic – a view confirmed by the extracted β_2 spectrum shown in the lower panel in Fig. 2(b), which displays an average value of $\beta_2 \approx 0$ throughout the range corresponding to the dominant channel 2 feature ($4000 \leq TKER \leq 8000$ cm^{-1}). The signal at higher TKER, where the channel 1 contribution would be expected, is too weak to allow extraction of reliable β_2 values. A discussion of the contrasting β_2 values of the ns and fs VMI measurements is, for completeness, provided in the ESI†, but we note that it is not central to any of the key arguments in the ensuing discussion.

3.2 Mechanism of $^1n\sigma^*$ mediated dissociation from $^1\pi\pi^*(\nu = 0)$

We now consider the mechanism of S–CH_3 bond cleavage on the $^1n\sigma^*$ PES following excitation at 289.8 nm. Central to this discussion is the energy barrier under the $^1\pi\pi^*/^1n\sigma^*$ CI, which will preclude dissociation from the $^1\pi\pi^*(\nu = 0)$ level when the S–CH_3 bond lies in the plane of the ring. The earlier VMI study[9] proposed that this CI (CI1′ in Fig. 1) lies ~722 cm^{-1} above the $^1\pi\pi^*(\nu = 0)$ level when the torsional angle $\phi = 0°$ (see inset to Fig. 1 for a depiction of the angle ϕ). Yet, the present fs and ns imaging studies at 289.8 nm, and those reported in ref. 9, all demonstrate that coupling from $^1\pi\pi^*(\nu = 0)$ onto the $^1n\sigma^*$ PES is an active process. O–H bond rupture following excitation of phenol (C_6H_5OH) at energies below an analogous $^1\pi\pi^*/^1\pi\sigma^*$ CI has been rationalized in terms of H-atom tunneling along the O–H bond fission coordinate,[15,29–31] but could such a mechanism apply in thioanisole given the 15-times heavier mass of the CH_3 group?

CASSCF calculations suggest an explanation for these observations. These show that the minimum energy geometry of the $^1\pi\pi^*$ state ($^1\pi\pi^*_{min}$) is similar to that of the S_0 state ($S_{0\ min}$). Both involve $\phi = 0°$ and $R_{S–CH_3} = 1.8$ Å, as shown in the ESI† (Fig. S4). Additionally, $^1\pi\pi^*_{min}$ shows some minor expansion of the phenyl ring following $^1\pi\pi^* \leftarrow S_0$ excitation, as expected for a ring-localized $\pi^* \leftarrow \pi$ excitation. These structures are consistent with previous findings from combined dispersed fluorescence and *ab initio* studies.[32] Further exploration of the excited state PESs using CASSCF locates a degeneracy between the $^1\pi\pi^*$ and the $^1n\sigma^*$ PESs at $R_{S–CH_3} \approx 2.1$ Å and $\phi = 0°$, corresponding to CI1′ in Fig. 1. This calculated CI1′ geometry is presented in Fig. 3(a). The present analysis also finds a second (lower energy) CI between the $^1\pi\pi^*$ and $^1n\sigma^*$ PESs at $R_{S–CH_3} \approx 2.1$ Å and $\phi = 90°$, and that the energy separation between the $^1\pi\pi^*$ and $^1n\sigma^*$ PESs is small ($\Delta E < 300$ cm^{-1}) at all intermediate values of ϕ. Henceforth, we therefore view CI1′ as a maximum on what is effectively a quasi-seam of intersection

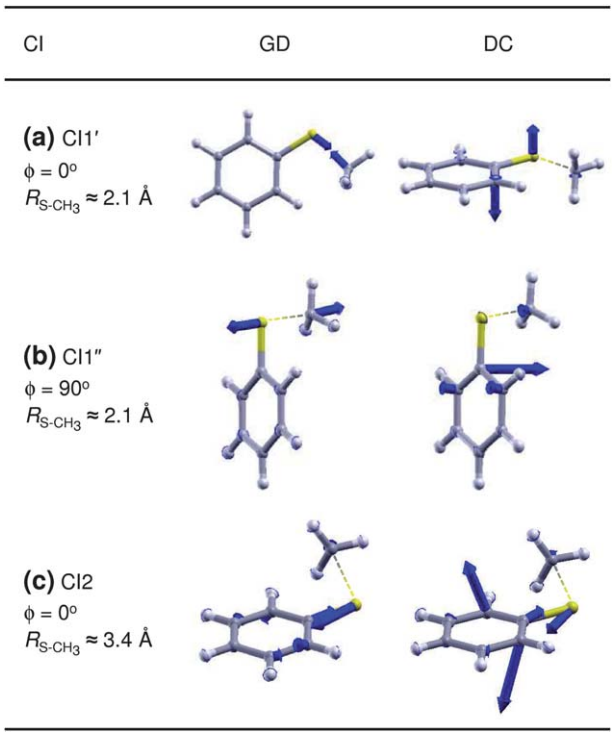

Fig. 3 Calculated geometries for (a) CI1′, (b) CI1″ and (c) CI2 at the CASSCF(10,9)/6-311G(d) level. Calculated GD and DC branching space motions are shown by the blue arrows.

between the $^1\pi\pi^*$ and $^1n\sigma^*$ PESs running along the ϕ-plane at $R_{S\text{–}CH_3} \approx 2.1$ Å, the minimum of which lies at (or close to) $\phi = 90°$. We denote this as a quasi-seam rather than an actual seam as the first-order non-adiabatic coupling along the torsion mode is non-zero, although very small, resulting in very weakly avoided potentials at intermediate ϕ (*vide infra*). Fig. 3(b) presents the CASSCF calculated minimum of this quasi-seam, designated CI1″, and correspondingly labeled on the potentials in Fig. 1. These findings allow a more coherent explanation of the photoinduced S–CH_3 bond fission dynamics following excitation to the $^1\pi\pi^*(\nu = 0)$ level.

The reported fluorescence lifetime of $^1\pi\pi^*(\nu = 0)$ molecules is ~2 ns, and the $^1\pi\pi^*(\nu = 0) \leftarrow S_0$ band shows resolved rotational fine structure,[32] implying that coupling from $^1\pi\pi^*(\nu = 0)$ to the $^1n\sigma^*$ PES is an inefficient process. Dissociation at $\phi = 0°$ is assumed to be closed, by virtue of the CI1′ barrier. But the $^1\pi\pi^*(\nu = 0)$ wavefunction spans a range of ϕ, the extremities of which (in ϕ) will encompass geometries closer to that of the minimum of the $^1\pi\pi^*/^1n\sigma^*$ CI quasi-seam (*i.e.* towards CI1″). Given the available potentials and the low transfer probabilities, we conclude that 'classically forbidden' regions of the $^1\pi\pi^*/^1n\sigma^*$ CI quasi-seam with $\phi \gg 0°$ play a defining role in allowing S–CH_3 bond fission from $^1\pi\pi^*(\nu = 0)$, but recognize that any detailed rationale for such low radiationless transition probabilities will require more accurate multi-dimensional PESs. Nonetheless, this conclusion implies that this bond fission must be visualized as a quantum mechanical phenomenon enabled by overlap of the bound $^1\pi\pi^*(\nu = 0)$ and $^1n\sigma^*$ continuum wavefunctions at large ϕ (*i.e.* as a tunneling process, but in a multi-dimensional (ϕ, $R_{S\text{–}CH_3}$, *etc.*) space).

The above interpretation for $^1n\sigma^*$ mediated S–CH_3 bond scission from $^1\pi\pi^*(\nu = 0)$ also helps to explain the observed dominance of adiabatic dissociation dynamics into channel 2 around CI2, the calculated geometric minimum for which involves $\phi = 0°$ at $R_{S\text{–}CH_3} \approx 3.4$ Å, as presented in Fig. 3(c). CASSCF calculations also indicate that, unlike the $^1\pi\pi^*/^1n\sigma^*$ CI quasi-seam, CI2 exhibits a shallow localized conical topography in the $R_{S\text{–}CH_3}/\phi$ plane, as verified by further CI searches which failed to locate any degeneracy between $^1n\sigma^*$ and S_0 when $\phi \neq 0°$ (see ESI†). Following the necessary torsional motion in $^1\pi\pi^*$ to enable coupling onto the $^1n\sigma^*$ PES at $\phi > 0°$ (nearer CI1″), the initial geometry on the latter PES will be far from that required to sample CI2. Given that $R_{S\text{–}CH_3}$ increases by ~1.3 Å from the $^1\pi\pi^*/^1n\sigma^*$ CI to CI2 along the repulsive $^1n\sigma^*$ PES and assuming formation of channel 2 photoproducts with an average TKER of ~6000 cm^{-1}, one can estimate a timescale of ~40 to 50 fs to reach CI2 on the $^1n\sigma^*$ PES.[21] This limits the possibility for further torsional rearrangement within the dissociating molecule. Further, the shallow topography of the $^1n\sigma^*/S_0$ CI (see ESI†) means that dissociating flux is unlikely to experience any appreciable force from the adiabatic PES to access the CI2 geometry, effectively avoiding the point of $^1n\sigma^*/S_0$ degeneracy. Ergo, one predominantly observes adiabatic dissociation into channel 2, shown by the solid black arrow in Fig. 1, and a much lower probability for non-adiabatic coupling into channel 1 at CI2.

3.3 Nature of the dynamic resonance at $^1\pi\pi^*(\nu_{7a} = 1)$

Previous ns photolysis experiments demonstrated that the branching between channel 1 and channel 2 photoproducts can be tuned by exciting a particular $^1\pi\pi^*$ vibrational level involving one quantum of ν_{7a}.[9] We have also performed ns imaging experiments following excitation of this 'dynamical resonance' at 283.9 nm, the results of which are presented in Fig. 4(a). The measured velocity map image (inset) and the TKER spectrum derived therefrom (open circles) both clearly confirm the enhanced propensity for non-adiabatic S–CH_3 bond fission through CI2 into channel 1 products; predicted $TKER_{max}(\tilde{X})$ and $TKER_{max}(\tilde{A})$ values based on the improved D_0(S–CH_3) value are shown by the vertical red and blue arrows, respectively, in Fig. 4(a). Analysis yields a branching ratio of $\Gamma \sim 0.4$ between channel 1 : channel 2 photoproducts (see ESI† for fitting details of the TKER spectrum in Fig. 4(a)), in excellent agreement with the value determined in the earlier study by Lim and Kim.[9]

The earlier study[9] reported a marked variation in the recoil anisotropy parameter of the channel 1 products (evolving from negative to positive β_2 as the TKER decreased from ~11 000 to ~9000 cm^{-1}), which inspired a suggestion that ν_{7a} stretching motion created a superposition of both $^1\pi\pi^*$ and $^1n\sigma^*$ states (whose transition dipole moments (TDMs) are orthogonal to one another – see Fig. S7), specifically localized at the nuclear geometry of CI1′. Given that the $^1n\sigma^* \leftarrow S_0$ TDM is oriented perpendicular to the plane of the phenyl ring (and to the S–CH_3 bond when at $S_{0\ min}$), it was plausible to associate the high energy tail of the channel 1 feature (at TKER >10 000 cm^{-1} and

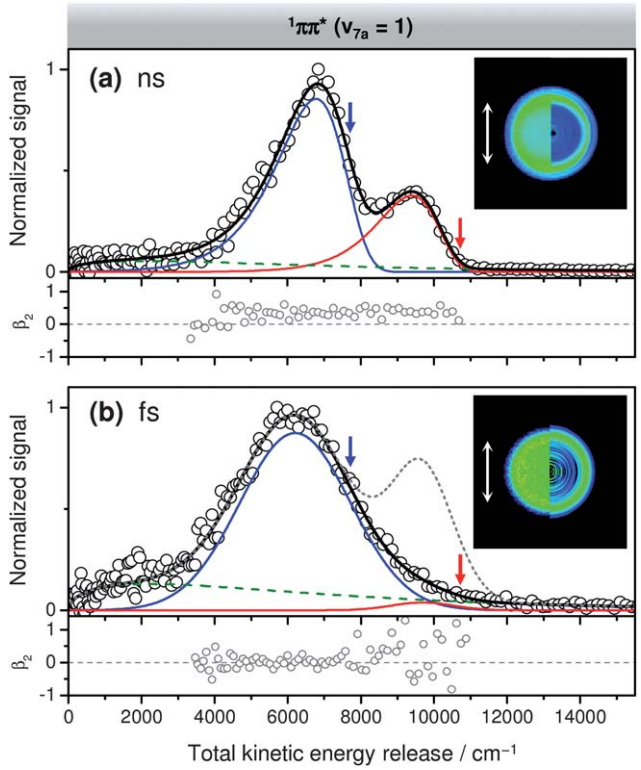

Fig. 4 TKER spectra obtained following photoexcitation of thioanisole with (a) ns and (b) fs pulses centered at 283.9 nm (*i.e.* on the $^1\pi\pi^*(\nu_{7a} = 1)$ resonance) and REMPI probing the CH_3 radical products, recorded at Δt = 20 and 1.2 ns, respectively. All other details are as for Fig. 2.

with $\beta_2 < 0$) with flux that propagated through CI1′ and down the $^1n\sigma^*$ PES at $\phi \approx 0°$ towards (and through) CI2 to channel 1 products (dashed arrows labeled ν_{7a} in Fig. 1). However, the present ns images show no such variation in β_2 across the channel 1 feature, as shown in the lower panel of Fig. 4(a). Rather, we find a consistently positive β_2 value of ~0.4, in-line with initial excitation solely to the $^1\pi\pi^*$ state. As noted earlier, the (near) complete elimination of underlying 'Boltzmann-like' signal in the present ns images (dashed green line in Fig. 4(a)) instils confidence in the β_2 values determined for the features associated with channel 1 and 2.

Given the above findings, we now explore the alternative view that the dynamics observed following excitation to the $^1\pi\pi^*(\nu_{7a} = 1)$ level may originate exclusively from the $^1\pi\pi^*$ state. Again, further guidance for understanding this process comes from our CASSCF calculations of the CIs, which also generate the pairs of nuclear motions (the branching space) responsible for lifting the electronic state degeneracy at the calculated CIs, while the degeneracy is conserved in the remaining $3N - 8$ vibrational degrees of freedom (N = number of atoms).[1] The modes of interest correlate to the gradient of the energy difference (GD) between the two electronic states and the derivative coupling (DC) which is parallel to the non-adiabatic coupling. The latter of these is the true non-Born–Oppenheimer term and is nominally responsible for facilitating vibronic (non-adiabatic) coupling between two electronic surfaces *via* a CI.[1] Branching space vibrations at all three calculated CI geometries are provided in Fig. 3 (blue arrows). If C_s symmetry is imposed (geometric and electronic) at CI1′, one finds that the GD vector corresponds to the S–CH_3 stretching motion (a'), while the DC vector corresponds to the anti-symmetric torsion motion along ϕ (a''). Crucially however, the magnitude of the DC vector is several orders of magnitude smaller than the GD vector resulting in a highly elliptical CI. As such, the degeneracy is barely lifted *via* motion in the DC direction compared to that along the GD. This can be further seen when symmetry constraints are removed in the calculations (*i.e.* C_s symmetry is broken), and one finds that the branching spaces collapse to a one-dimensional sub-space, composed exclusively of the S–CH_3 stretch motion, where the GD and DC are essentially collinear and of opposite phase, forming a linearly-dependent set (see branching spaces in Fig. S8). At all intermediate torsion angles ($0° < \phi < 90°$), constrained CI geometry optimizations find near degeneracies (very weakly avoided crossings; $\Delta E < 300$ cm^{-1}) and we can thus envisage a quasi-seam connecting the CI1′ ($\phi = 0°$) and CI1″ ($\phi = 90°$) geometries (both with C_s symmetry). Thus, quite remarkably, in the absence of C_s symmetry ($0° < \phi < 90°$), to first-order, only motion in the S–CH_3 stretch coordinate lifts the quasi-degeneracy between the $^1\pi\pi^*$ and $^1n\sigma^*$ states. This type of CI topography is rather rare, but has been observed previously in guanine–cytosine DNA base pairs.[33]

The present finding offers significantly deeper insight into the dynamical origins of the 722 cm^{-1} resonance-specific product branching seen in Fig. 4(a). C_s symmetry dictates that coupling between the $^1\pi\pi^*(A')$ and $^1n\sigma^*(A'')$ states through CI1′ can, in principle, be mediated by the anti-symmetric (a'') torsion motion in ϕ (DC), but not by the symmetric (a') S–CH_3 stretching motion (GD); $A' \otimes a'' \otimes A'' \supset A'$. Yet, the present calculations also reveal that the small magnitude of DC (relative to GD) makes non-adiabatic coupling between the $^1\pi\pi^*$ and $^1n\sigma^*$ states at $\phi = 0°$ very weak. When C_s symmetry is broken ($0° < \phi < 90°$) however, motion in the S–CH_3 stretch coordinate becomes solely responsible for driving $^1\pi\pi^* \rightarrow {}^1n\sigma^*$ population transfer. Thus, the most straightforward rationale within the context of the PESs shown in Fig. 1 is to recognize that the $^1\pi\pi^*(\nu_{7a} = 1)$ wavefunction also spans a range of ϕ and that passage through the $^1\pi\pi^*/{}^1n\sigma^*$ CI quasi-seam is most efficient at non-planar geometries. The increased branching into channel 1 products is primarily a reflection of the fact that excitation in ν_{7a} enables access to the $^1n\sigma^*$ PES at smaller ϕ, and so a larger fraction of the flux dissociating on the $^1n\sigma^*$ PES samples CI2 at larger R_{S-CH_3} (and $\phi \approx 0°$).

Broadband excitation with fs pulses centered at ~283.9 nm results in no observable enhancement into channel 1, as shown by the TKER spectrum (open circles) presented in Fig. 4(b). A fit to this spectrum (black line) suggests that only ~2% of the total reactive flux excited with the broadband pulse evolves into channel 1 (very similar to that found when exciting around $^1\pi\pi^*(\nu = 0)$, Fig. 2(b)). By way of illustration, the dotted grey line in Fig. 4(b) shows the 'predicted' profile of the fs TKER spectrum if all excited molecules displayed the same dynamics as those prepared by ns excitation at the same centre wavelength. The absence of the photoproduct branching resonance in the fs imaging study is unsurprising, since the broadband fs

excitation prepares flux across a superposition of vibrational levels,[34] whereas with a narrowband ns pulse the reactive flux can be localized into the required control coordinate. To this end, the fs results in Fig. 4(b) further serve to emphasize the mode specific nature of the photoproduct branching resonance at 283.9 nm.

3.4 Timescales for $^1n\sigma^*$ mediated S–CH_3 bond fission

Fig. 5(a) illustrates the timescales for S–CH_3 bond fission into channel 2 photoproducts in a more quantitative manner. It displays normalized CH_3^+ signal transients of integrated channel 2 features (circles), measured by fs TR-VMI at five different pump wavelengths, out to the temporal limits of the experiment ($\Delta t = 1.2$ ns): 289.8 (green), 286.8 (blue), 283.9 (red), 279 (orange) and 275 nm (grey). These CH_3^+ transients are generated by obtaining a series of fs TKER spectra from velocity map images recorded at different Δt, and then integrating signal in a 2000 cm^{-1} window straddling the center of the channel 2 feature. All of the individual fs images (and the associated TKER spectra) recorded at $\Delta t = 1.2$ ns at all of these wavelengths are dominated by the feature associated with channel 2 products (Fig. S2), analogous to Fig. 2(b) and 4(b). All transients in Fig. 5(a) show a sharp rise in signal at $\Delta t =$ 0 picoseconds (ps), which is associated with the underlying 'Boltzmann-like' signal in the fs TKER spectra. Beyond $\Delta t > 1$ ps, the transients show that: (i) the overall dissociation process into channel 2 occurs over a timeframe of hundreds to thousands of picoseconds; and (ii) the rate of S−CH_3 bond fission increases with increasing internal (vibrational) energy in the $^1\pi\pi^*$ state (*i.e.* with increasing $h\nu_{pu}$ energy). Kinetic fits to these temporal profiles using exponential rise functions convoluted with our Gaussian instrument function (~120 fs) yield the solid lines in Fig. 5(a) (see ESI† for fitting details). These fits return time constants (τ) for adiabatic dissociation to channel 2 products of 1430 ± 240, 840 ± 100, 670 ± 50, 189 ± 10 and 74 ± 10 ps for excitation centered at 289.8, 286.8, 283.9, 279 and 275 nm, respectively. These τ values, together with the corresponding dissociation rate constants ($k = 1/\tau$), are summarized in Table 1 and correlate to the timescales for forming channel 2 photoproducts.

Table 1 Adiabatic S–CH_3 dissociation time constants (τ) and associated dissociation rates ($k = 1/\tau$) obtained from kinetic fits to the CH_3^+ signal transients presented in Fig. 5(a). Errors correspond to 2 standard deviations (2 sigma)

λ/nm	$^1\pi\pi^*$ excess internal energy[a]/cm^{-1}	τ/ps	$k/10^9$ s^{-1}
289.8	0	1430 ± 240	0.70 ± 0.12
286.8	360	840 ± 100	1.19 ± 0.14
283.9	720	670 ± 50	1.49 ± 0.11
279	1340	189 ± 10	5.29 ± 0.28
275	1860	74 ± 10	13.5 ± 1.83

[a] Values given are mean excess energies.

The rate constant for S–CH_3 bond fission, k, (Table 1 and red circles, Fig. 5(b)) increases with increasing (vibrational) excitation within the $^1\pi\pi^*$ manifold, but even at 275 nm the dissociation time constants are all on the order of picoseconds – timescales traditionally associated with intramolecular vibrational energy redistribution (IVR) in small aromatic species.[35] Given this finding, and the observation that the fs TKER spectra recorded at all $h\nu_{pu}$ energies are dominated by channel 2 products, we recall the earlier conclusions that the minimum energy pathways through the $^1\pi\pi^*/^1n\sigma^*$ CI quasi-seam involve non-planar geometries ($\phi \neq 0°$). $^1\pi\pi^* \leftarrow S_0$ excitation populates Franck–Condon active modes in the $^1\pi\pi^*$ state. These are predominantly ring-breathing modes, involving motions that are orthogonal to both the S–CH_3 dissociation coordinate and to the torsional (ϕ) coordinate. Energy localized in such modes will be of little benefit in accessing the $^1\pi\pi^*/^1n\sigma^*$ CI quasi-seam, but the anharmonicity of the $^1\pi\pi^*$ PES will encourage IVR – to an extent that increases with excitation energy. Thus the observed increase in k with increasing $h\nu_{pu}$ can be understood in terms of the expanding area of configuration space

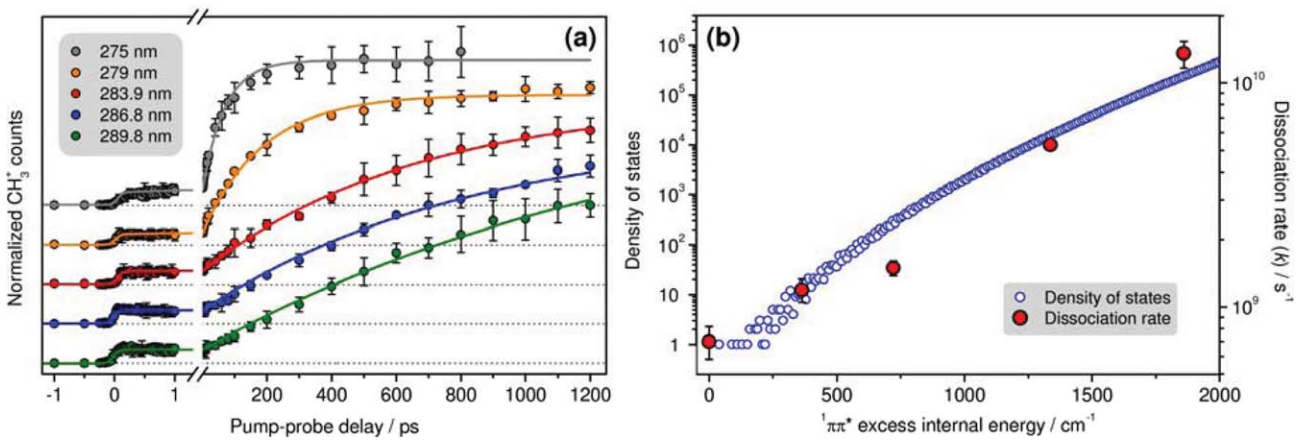

Fig. 5 (a) Normalized integrated CH_3^+ signal transients for channel 2 features (circles) from fs TR-VMI following excitation centered at 289.8 (green), 286.8 (blue), 283.9 (red), 279 (orange) and 275 nm (grey) plotted as a function of pump-probe delay. Error bars correspond to 2 standard deviations in the mean signal values, and the solid lines show kinetic fits (see ESI†). (b) Dissociation rate ($k = 1/\tau$) as a function of mean internal (vibrational) energy imparted to the $^1\pi\pi^*$ molecules by photoexcitation (red circles), compared to the calculated density of vibrational states in the $^1\pi\pi^*$ state at 25 cm^{-1} energy intervals (blue circles).

(especially in the ϕ and/or ν_{7a} coordinates) sampled by the excited $^1\pi\pi^*$ molecules. Further support for this mechanism is provided by noting the broadly similar $h\nu_{pu}$ dependences of k and the calculated density of vibrational states in $^1\pi\pi^*$ (blue circles in Fig. 5(b)) – the latter were derived (at 25 cm^{-1} energy intervals) from the calculated CASSCF harmonic frequencies in the $^1\pi\pi^*$ state (from the structure presented in Fig. S4(b)) using an extended Beyer-Swinehart method described in ref. 36.

4 Conclusions

By performing a combination of ns VMI, fs TR-VMI and high level *ab initio* calculations, new detailed insight into the $^1n\sigma^*$ mediated S–CH_3 fission dynamics in thioanisole has been achieved. In particular, these studies more clearly elucidate (i) the origins of mode-specific enhanced coupling through the $^1\pi\pi^*/^1n\sigma^*$ CI following excitation to the ν_{7a} (S–CH_3 stretch) level in the $^1\pi\pi^*$ state, and (ii) the mechanism for S–CH_3 bond fission cleavage *via* $^1n\sigma^*$ following excitation to the $^1\pi\pi^*(\nu = 0)$ level, which is viewed as a closed pathway at planar geometries by virtue of the size of the barrier under the $^1\pi\pi^*/^1n\sigma^*$ CI. Guided by findings from *ab initio* calculations, these issues are considered in a reduced sub-set of two (of the total $3N - 6$ available) vibrational degrees of freedom: the S–CH_3 stretch and the torsion of the S–CH_3 group with respect to the phenyl ring plane (defined by the angle ϕ). Following initial excitation to $^1\pi\pi^*(\nu = 0)$ at planar geometries, the nuclear framework evolves to sample a wider range of ϕ, including regions at larger ϕ where the barrier associated with the $^1\pi\pi^*/^1n\sigma^*$ CI is smaller. Non-adiabatic coupling to the dissociative $^1n\sigma^*$ PES is deduced to occur only at the 'classically forbidden' extremities of the $^1\pi\pi^*(\nu = 0)$ wavefunction (*i.e.* at far from planar geometries with $\phi \neq 0^\circ$). The present calculations reveal that motion in the S–CH_3 stretch coordinate encourages non-adiabatic population transfer through the $^1\pi\pi^*/^1n\sigma^*$ CI at ϕ values closer to 0°, manifesting as a striking modification of the photoproduct branching ratio (relative to other excitation wavelengths) when a single quantum of ν_{7a} is populated in the $^1\pi\pi^*$ state.

From a broader perspective, the dynamics observed in thioanisole, together with tunneling dynamics in phenols,[15,29–31] serve as exemplars of the pivotal role purely quantum phenomena can play in driving σ^* mediated photochemistry. Moreover, and perhaps most significant, it also offers an extremely elegant demonstration that, by understanding key attributes of an excited state potential energy landscape with quantum calculations (such as the nuclear motions required for promoting coupling through CIs), one can indeed translate this into a strategy for experimental control over fundamental photochemistry – one of the keystones for a vision of 'quantum control' of chemical reactions at a molecular level.

Acknowledgements

M.J.P. and L.T.B. thank the European Research Council for funding. A.M.W., S.J.H., T.N.V.K. and M.N.R.A. thank the Engineering and Physical Sciences Research Council (EPSRC), the Marie Curie Initial Training Network ICONIC and the Royal Society Leverhulme Trust Senior Research Fellowship Scheme for funding. G.M.R., D.J.H. and V.G.S. thank the EPSRC, the Leverhulme Trust and the Royal Society for funding. The authors are grateful to Dr T.A.A. Oliver for stimulating discussions and to D. Zaouris and M.I. Cotterell for their contributions to the ns work.

References

1 D. R. Yarkony, *Rev. Mod. Phys.*, 1996, **68**, 985–1013.
2 *Conical Intersections: Theory, Computation and Experiment*, ed. W. Domcke, D. R. Yarkony and H. Koppel, World Scientific Publishing Co. Pte. Ltd., Singapore, 2011.
3 A. L. Sobolewski, W. Domcke, C. Dedonder-Lardeux and C. Jouvet, *Phys. Chem. Chem. Phys.*, 2002, **4**, 1093–1100.
4 M. N. R. Ashfold, G. A. King, D. Murdock, M. G. D. Nix, T. A. A. Oliver and A. G. Sage, *Phys. Chem. Chem. Phys.*, 2010, **12**, 1218–1238.
5 C. E. Crespo-Hernandez, B. Cohen, P. M. Hare and B. Kohler, *Chem. Rev.*, 2004, **104**, 1977–2019.
6 A. G. Sage, M. G. D. Nix and M. N. R. Ashfold, *Chem. Phys.*, 2008, **347**, 300–308.
7 A. G. Sage, T. A. A. Oliver, D. Murdock, M. B. Crow, G. A. D. Ritchie, J. N. Harvey and M. N. R. Ashfold, *Phys. Chem. Chem. Phys.*, 2011, **13**, 8075–8093.
8 D. J. Hadden, C. A. Williams, G. M. Roberts and V. G. Stavros, *Phys. Chem. Chem. Phys.*, 2011, **13**, 4494–4499.
9 J. S. Lim and S. K. Kim, *Nat. Chem.*, 2010, **2**, 627–632.
10 T. A. A. Oliver, G. A. King, D. P. Tew, R. N. Dixon and M. N. R. Ashfold, *J. Phys. Chem. A*, 2012, DOI: 10.1021/jp308804d.
11 M. N. R. Ashfold, A. L. Devine, R. N. Dixon, G. A. King, M. G. D. Nix and T. A. A. Oliver, *Proc. Natl. Acad. Sci. U. S. A.*, 2008, **105**, 12701–12706.
12 A. L. Devine, M. G. D. Nix, R. N. Dixon and M. N. R. Ashfold, *J. Phys. Chem. A*, 2008, **112**, 9563–9574.
13 J. S. Lim, Y. S. Lee and S. K. Kim, *Angew. Chem., Int. Ed.*, 2008, **47**, 1853–1856.
14 T. A. A. Oliver, Y. Zhang, M. N. R. Ashfold and S. E. Bradforth, *Faraday Discuss.*, 2011, **150**, 439–458.
15 Y. Zhang, T. A. A. Oliver, M. N. R. Ashfold and S. E. Bradforth, *Faraday Discuss.*, 2012, **157**, 141–163.
16 S. C. Althorpe, in *Conical Intersections: Theory, Computation and Experiment*, ed. W. Domcke, D. R. Yarkony and H. Koppel, World Scientific Publishing Co. Pte. Ltd., Singapore, 2011, ch. 4, pp. 155–194.
17 G. Varsányi, *Assignments for vibrational spectra of 700 benzene derivatives*, Wiley, New York, 1974.
18 M. L. Hause, Y. H. Yoon and F. F. Crim, *J. Chem. Phys.*, 2006, **125**, 174309.
19 M. L. Hause, Y. H. Yoon and F. F. Crim, *Mol. Phys.*, 2008, **106**, 1127–1133.
20 M. L. Hause, Y. H. Yoon, A. S. Case and F. F. Crim, *J. Chem. Phys.*, 2008, **128**, 104307.
21 C. A. Williams, G. M. Roberts, H. Yu, N. L. Evans, S. Ullrich and V. G. Stavros, *J. Phys. Chem. A*, 2012, **116**, 2600–2609.
22 E. Wrede, S. Laubach, S. Schulenburg, A. Brown, E. R. Wouters, A. J. Orr-Ewing and M. N. R. Ashfold, *J. Chem. Phys.*, 2001, **114**, 2629–2646.

23 A. T. J. B. Eppink and D. H. Parker, *Rev. Sci. Instrum.*, 1997, **68**, 3477–3484.
24 J. W. Hudgens, T. G. Digiuseppe and M. C. Lin, *J. Chem. Phys.*, 1983, **79**, 571–582.
25 G. M. Roberts, J. L. Nixon, J. Lecointre, E. Wrede and J. R. R. Verlet, *Rev. Sci. Instrum.*, 2009, **80**, 053104.
26 M. J. Frisch, G. W. Trucks, H. B. Schlegel, G. E. Scuseria, M. A. Robb, J. R. Cheeseman, J. A. Montgomery, Jr, T. Vreven, K. N. Kudin, J. C. Burant, J. M. Millam, S. S. Iyengar, J. Tomasi, V. Barone, B. Mennucci, M. Cossi, G. Scalmani, N. Rega, G. A. Petersson, H. Nakatsuji, M. Hada, M. Ehara, K. Toyota, R. Fukuda, J. Hasegawa, M. Ishida, T. Nakajima, Y. Honda, O. Kitao, H. Nakai, M. Klene, X. Li, J. E. Knox, H. P. Hratchian, J. B. Cross, V. Bakken, C. Adamo, J. Jaramillo, R. Gomperts, R. E. Stratmann, O. Yazyev, A. J. Austin, R. Cammi, C. Pomelli, J. W. Ochterski, P. Y. Ayala, K. Morokuma, G. A. Voth, P. Salvador, J. J. Dannenberg, V. G. Zakrzewski, S. Dapprich, A. D. Daniels, M. C. Strain, O. Farkas, D. K. Malick, A. D. Rabuck, K. Raghavachari, J. B. Foresman, J. V. Ortiz, Q. Cui, A. G. Baboul, S. Clifford, J. Cioslowski, B. B. Stefanov, G. Liu, A. Liashenko, P. Piskorz, I. Komaromi, R. L. Martin, D. J. Fox, T. Keith, M. A. Al-Laham, C. Y. Peng, A. Nanayakkara, M. Challacombe, P. M. W. Gill, B. Johnson, W. Chen, M. W. Wong, C. Gonzalez, and J. A. Pople, *Gaussian 03, Revision D.01*, Gaussian, Inc., Wallingford CT, 2004.
27 J. B. Kim, T. I. Yacovitch, C. Hock and D. M. Neumark, *Phys. Chem. Chem. Phys.*, 2011, **13**, 17378–17383.
28 G. M. Roberts, C. A. Williams, M. J. Paterson, S. Ullrich and V. G. Stavros, *Chem. Sci.*, 2012, **3**, 1192–1199.
29 G. A. Pino, A. N. Oldani, E. Marceca, M. Fujii, S. I. Ishiuchi, M. Miyazaki, M. Broquier, C. Dedonder and C. Jouvet, *J. Chem. Phys.*, 2010, **133**, 124313.
30 R. N. Dixon, T. A. A. Oliver and M. N. R. Ashfold, *J. Chem. Phys.*, 2011, **134**, 194303.
31 G. M. Roberts, A. S. Chatterley, J. D. Young and V. G. Stavros, *J. Phys. Chem. Lett.*, 2012, **3**, 348–352.
32 M. Hoshino-Nagasaka, T. Suzuki, T. Ichimura, S. Kasahara, M. Baba and S. Kawauchi, *Phys. Chem. Chem. Phys.*, 2010, **12**, 13243–13247.
33 G. Groenhof, L. V. Schafer, M. Boggio-Pasqua, M. Goette, H. Grubmuller and M. A. Robb, *J. Am. Chem. Soc.*, 2007, **129**, 6812–6819.
34 A. H. Zewail, *J. Phys. Chem. A*, 2000, **104**, 5660–5694.
35 K. L. Reid, *Int. Rev. Phys. Chem.*, 2008, **27**, 607–628.
36 S. E. Stein and B. S. Rabinovitch, *J. Chem. Phys.*, 1973, **58**, 2438–2445.